Nuclear Instruments and Methods in Physics Research A 713 (2013) 40–51

Contents lists available at SciVerse ScienceDirect

Nuclear Instruments and Methods in Physics Research A

journal homepage: www.elsevier.com/locate/nima

Development of high-rate MRPCs for high resolution time-of-flight systems

Jingbo Wang [a], Yi Wang [a,*], D. Gonzalez-Diaz [a,b,c], Huangshan Chen [a], Xingming Fan [a], Yuanjing Li [a], Jianping Cheng [a], Marcus Kaspar [d], Roland Kotte [d], Alejandro Laso Garcia [d], Lothar Naumann [d], Daniel Stach [d], Christian Wendisch [d], Jörn Wüstenfeld [d]

[a] Department of Engineering Physics, Tsinghua University, Key Laboratory of Particle & Radiation Imaging, Ministry of Education, Beijing 100084, China
[b] GSI Helmholtz Center for Heavy Ion Research, Darmstadt, Germany
[c] Laboratorio de Física, Nucleary Altas Energías, Universidad de Zaragoza, Zaragoza, Spain
[d] Forschungszentrum Dresden-Rossendorf, Dresden, Germany

ARTICLE INFO

Article history:
Received 16 July 2012
Received in revised form
20 January 2013
Accepted 20 February 2013
Available online 6 March 2013

Keywords:
MRPC
TOF
CBM
High rate
Low-resistive glass
Rate capability

ABSTRACT

We show how the high charged-particle flux (1–20 kHz/cm^2) expected over the 150 m^2 large time-of-flight wall of the future Compressed Baryonic Matter experiment (CBM) at FAIR can be realistically handled with Multi-gap Resistive Plate Chambers (MRPCs). This crucial 100-fold increase of the chamber rate capability, as compared to that of standard MRPCs presently employed in experiments resorting to sub-100 ps timing, has been achieved thanks to the development of a new type of low-resistive doped glass. Following the encouraging results previously obtained with small counters, two types of modules (active area: $\sim$150 cm^2) have been built at Tsinghua University with the new material. The measurements conveyed in this work, obtained with a quasi- minimum ionizing electron beam ($\gamma\beta \geq 3$), prove their suitability as the building blocks of the present hadron-identification concept of the CBM experiment. Namely, they provide a time resolution better than 80 ps and an efficiency above 90% at a particle flux well in excess of 20 kHz/cm^2 (up to 35–60 kHz/cm^2), being at the core of a modular concept that is easily scalable. Recent measurements of the electrical and mechanical properties of this new material, together with its long-term behavior, are shortly summarized.

1. Introduction

Multi-gap Resistive Plate Chambers (MRPCs), first developed in 1996 [1], are spark-protected gaseous detectors with good time resolution, high efficiency and relatively low cost. During the last decade, thanks to the progress made in timing MRPCs [2–4], large-area time-of-flight systems have become widespread in modern nuclear and particle physics experiments, such as ALICE [5–7], STAR [8–10], FOPI [11,12], HADES [13,14], etc. Recent R&D efforts revealed that intrinsic detector resolutions down to 20 ps are possible under certain conditions [15]. Presently, the main drawback of these timing MRPCs is their limited capability to handle a ($\sim$minimum ionizing) charged particle flux exceeding some hundreds of Hz/cm^2, a fact that stems from the usage of conventional soda-lime float glass plates with a bulk resistivity in the range 10^{12}–10^{13} Ω cm. Hence, the insulation technique that endows the counter with its unique spark-quenching characteristics at very high uniform fields is ultimately responsible for the charge build-up process that effectively limits the operating field at high particle flux.

The next generation Compressed Baryonic Matter experiment (CBM) at the future Facility for Antiproton and Ion Research (FAIR) in Darmstadt, Germany, is planned to be built with a time-of-flight system based on MRPCs. The aim is to obtain good hadron identification in fixed-target heavy ion collisions at projectile energies up to E=25 GeV/A (for details see Ref. [17] and references therein). The challenge is to keep a high efficiency (above 90%) and a good time of flight resolution (better than 80 ps) at a particle flux up to 20 kHz/cm^2, which is not accessible to conventional float-glass MRPCs ([17], for instance). Thus, the task of finding materials capable of replacing float glass for timing applications but providing a much less resistive return path to the released charge has been the subject of intense R&D efforts in the recent years: notably, as shown in Ref. [16–25], the development of various types of semi-conductive glass, ceramics as well as the so called warm glass technology. The usage of semi-conductive glass, in particular, dates back to the Pestov counter (for an overview see Ref. [26] and references therein). Recently, at Tsinghua University, we have managed to develop a stable production line of a promising new type of doped glass. Following the encouraging results obtained with small-area MRPC prototypes based on this material [24], two MRPC modules were

* Corresponding author. Tel.: +86 1062771960; fax: +86 1062782658.
E-mail addresses: jingbo.phy@gmail.com (J. Wang), yiwang@mail.tsinghua.edu.cn (Y. Wang).

0168-9002/$ - see front matter © 2013 Elsevier B.V. All rights reserved.
http://dx.doi.org/10.1016/j.nima.2013.02.036

produced in order to suit the current design of the CBM–TOF wall. The counters have been thoroughly characterized with a 30 MeV electron beam at the Electron Linac with high Brilliance and low Emittance facility (ELBE) [25,27] at Helmholtz-Zentrum Dresden-Rossendorf (HZDR).

The present report is organized as follows: Section 2 describes the mechanical properties of the new low-resistive glass together with a short explanation of its electrical properties; Section 3 presents the two counters developed for the CBM–TOF wall; Section 4 describes the ELBE facility and the experimental setup; Section 5 presents the counters performance as a function of high voltage and particle flux; and Section 6 is devoted to a comprehensive comparison between present results and results previously obtained with a hadron beam uniformly irradiating the chamber. Finally, Section 7 summarizes our conclusions and outlook.

2. Low-resistive glass

This new glass, developed for high charged particle flux applications, is characterized by an ohmic behavior and stability with transported charge, properties that rely on a balanced admixture of oxides of transition elements [24]. It has a black color and it is opaque to visible light, as commonly attributed to glass exhibiting a form of electron conductivity. Its final conductivity turns out to be very sensitive to both the initial chemical composition of the raw material and to the glass melting procedure. Different compositions and related production procedures have been studied, yielding a tunable bulk resistivity in the range of 10^{10}–$10^{11}\ \Omega$ cm. Fig. 1 shows the measured bulk resistivity as a function of the position along a 30 cm-long glass plate, for a randomly selected sample. The measurements were done in a constant-temperature dry box where the temperature and the humidity could be controlled. At room temperature (25 °C) and a relative humidity of ~30%, the resistivity is seen to change within a mild 30% variation around an average value of $\rho = 1.5 \times 10^{10}\ \Omega$ cm. Deviations with respect to the results given in Ref. [24] stay within less than a factor of two and can be attributed mainly to sample-to-sample variations. The material exhibits a highly ohmic behavior up to 1 kV and follows Arrhenius law as a function of temperature, $\rho = \rho_{T_0} 10^{(T_0-T)/\Delta T}$ [24]. Strikingly, it shows one (potentially usable) order of magnitude resistance decrease every 28° (i.e., $\Delta T = 28$ °C), very close to the behavior previously reported for float glass [18,19]. Its dielectric constant in the GHz-range, measured both with capacitive and transmission line techniques, shows a value of $\varepsilon_r(1\ \text{GHz}) = 7.5$–$9.5$, just moderately higher than the one measured for float glass ($\varepsilon_r(1\ \text{GHz}) = 6 \pm 0.5$). Its loss-tangent $\tan\delta(1\ \text{GHz}) = 0.035$ is also comparable to the one measured for float glass $\tan\delta(1\ \text{GHz}) = 0.025 \pm 0.05$, [28]. Arguing along the lines of Ref. [28], neither we expected nor we observed any limitation for CBM counters coming from these modest deviations with respect to the values of float glass, either from the point of view of signal induction, transmission or cross-talk.

More importantly, this new low-resistive glass shows a large stability against electrical stress: under static conditions its breakdown field is above 1 kV/mm (a comfortable lower bound) and its resistivity increases within an acceptable factor of 2 for a density of transported charge as large as 1 C/cm^2 (over 34 days), a value close to the expected CBM live-time [17]. We have recently started ageing tests under dynamic conditions, i.e., directly on a (externally irradiated) RPC, and observed no discernible ageing effects up to 0.05 C/cm^2 (300 h). This figure, still much lower than the anticipated CBM live-time, does already exceed the operating live-times of so far existing timing MRPC walls. Details have been published elsewhere [29].

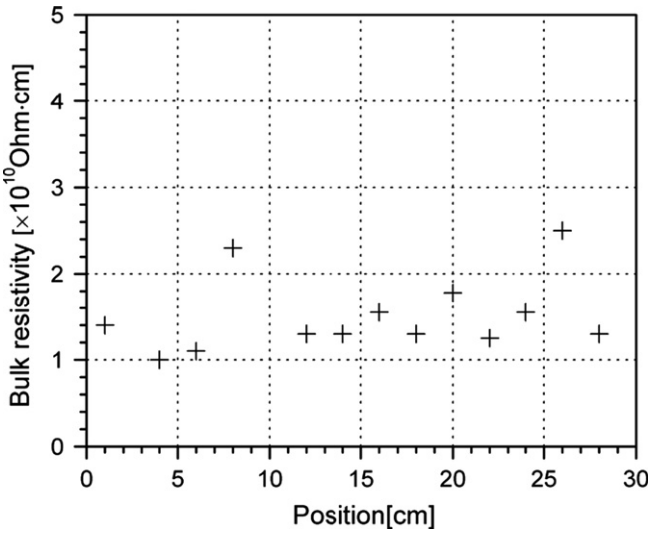

Fig. 1. Bulk resistivity of the low-resistive doped glass developed at Tsinghua University as a function of the position along a randomly selected sample (the dimensions of the plate are 20 cm × 30 cm × 0.11 cm). Temperature was around 25 °C.

As compared to the well-established float glass technology,[1] however, low-resistive glass production is in a less mature stage of development. Similar to the former, the technique of melting and annealing is very important in order to produce glass with high quality. But, contrary to float glass, the required surface quality of the low-resistive glass can be only achieved after a post-processing polishing process. The roughness of the electrode introduces local field variations which may deteriorate the efficiency and time resolution, [21,30]. It is believed that surface properties also determine the dark current and photon feedback levels [31]. Since a high surface quality is required by a high quality glass, surface measurements might be a key part of a protocol designed for the quality control of the glass mass production in order to consistently produce reliable glass. Here we report on the surface roughness of the glass plates, as determined by a MicroXAM 3D surface profiler that can measure the surface profile and the roughness of highly polished optical elements and rough surfaces, such as steel, paper, plastics, and ceramics. A 3-D scan image is shown in Fig. 2. The surface roughness can be expressed by a list of numbers following different definitions [32]. Three of the most commonly used definitions are shown under an evaluation scale of about 857 μm × 638 μm: average roughness (1.06 nm), peak–peak roughness (10.6 nm) and ten-point-height roughness (9.42 nm). For reference, the numbers for a float glass sample analyzed through the same procedure are 0.608/8.17/6.22.

3. Development of real-size modules

In the current CBM conceptual design, the whole TOF wall is arranged in four 'rate regions' [17]. In the inner region of the wall (region 1), pad readout MRPCs based on low-resistive glass can be efficiently used to cope with the high particle flux (up to 20 kHz/cm^2) at an optimal segmentation (4–6 cm^2/pad), while strip-readout MRPCs represent a natural choice for the outer region (0.5–8 kHz/cm^2) where the system occupancy and flux are orders of lower magnitude.

Recently, our effort is to realistically adapt the MRPC geometry to suit the conceptual design of the TOF wall, as of Ref. [17].

[1] Less often named soda-lime or window glass technology.

For region 1, the simulated particle flux ranges from 8 kHz/cm^2 to 25 kHz/cm^2 and the particle density, obtained for the most stringent central Au–Au collisions at 25 GeV/A, reaches a maximum value of about 0.01/cm^2. Hence, a small-pad MRPC (PMRPC), that could constitute the core of a future super-module, has been developed (Fig. 3-up). The counter has 10 gas gaps and consists of two (mirrored) stacks of plates made of 0.7 mm-thick low-resistive glass with a resistivity of about $2\times10^{10}\,\Omega$ cm. It has 6×2 pads of size 2 cm $\times$ 2 cm each, with an interval between pads of 2 mm (occupancy $<5\%$). The gas gap is 0.22 mm, defined by nylon monofilaments. The high voltage electrodes are covered with colloidal graphite spray, yielding a typical surface resistivity of about 2 MΩ/sq.

In view of their much lower occupancy rate regions 2, 3 and 4 of the TOF wall are currently foreseen to be assembled with multi-strip counters. The structure of the strip-readout MRPC proposed here is depicted in Fig. 4. As for the pad counter, it can be considered as a super-imposed structure of two 5-gap MRPCs mirrored with respect to one of the electrodes, that allows to easily provide the same (negative here) HV to 'both' chambers. The positive HV is applied to the outer electrodes. As compared to the pad-design, the strip-counter has slightly larger gaps of 0.25 mm aimed at partially compensating for the lower signal levels characterized by the strip designs. The readout strips have 24 cm length and 2.2 cm width. The intervals between the strips are 3 mm, in which grounded guard strips connected with vias have been patterned, for crosstalk minimization. A possible layout based on this type of modules was described in some detail in Ref. [33].

In both modules, similarly to the 10-gap counter in Ref. [24], signals induced with both polarities are sent in differential fashion to the front end electronics (FEE) used for the STAR TOF prototype 'TOFr' [34] in RHIC Run 3. This FEE is described in Ref. [35].

The working gas is a mixture of 85% $C_2H_2F_4$, 5% iso-C_4H_{10} and 10% SF_6 at nearly atmospheric pressure.

4. Beam test at ELBE

4.1. The ELBE electron beam

The ELBE facility at Helmholtz-Zentrum Dresden-Rossendorf, Dresden, Germany, consists of a 250 keV thermionic electron gun providing a pulsed electron beam. It is followed by a two-stage superconducting linear accelerator (Linac) consisting of four cavities, each allowing for an energy gain of 10 MeV. The accelerator produces a quasi-continuous electron beam with a tunable micro-pulse repetition rate of 26 MHz/2^{Nmp} (N_{mp}=1, 2, …,8) and

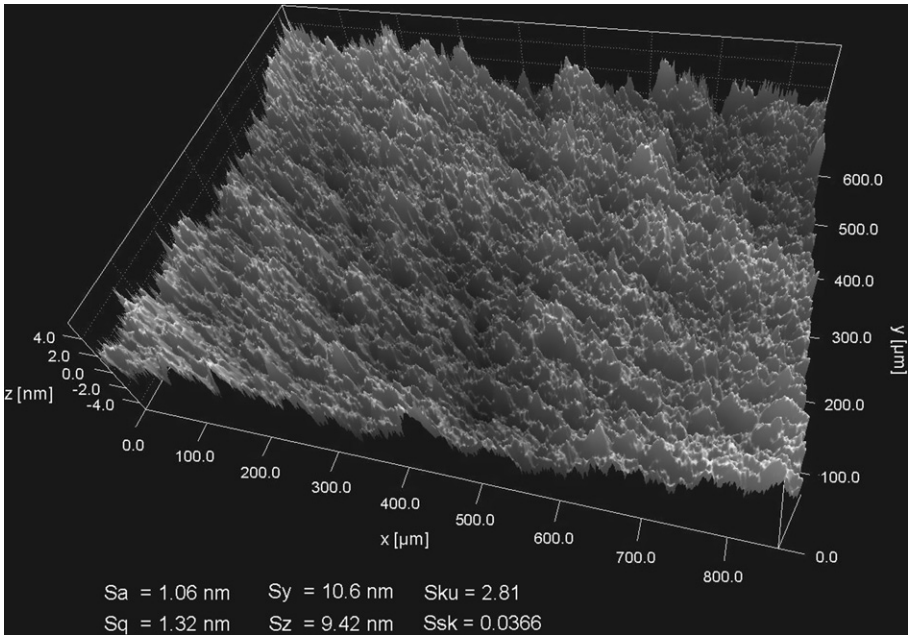

Fig. 2. 3-D image of the surface of the low-resistive glass: *Sa* (average roughness), *Sq* (root-mean-square roughness), *Sy* (peak-peak roughness), *Sz* (ten-point-height roughness), *Sku* (surface-kurtosis roughness) and *Ssk* (surface-skewness roughness) are used to evaluate the surface roughness.

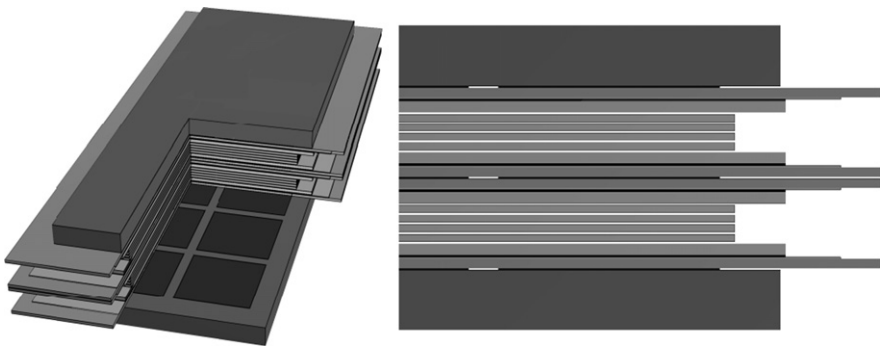

Fig. 3. Pad-readout MRPC, featuring a 10-gap 6×2-pad structure.

a corresponding bunch duration of less than 5 ps. A description of the experimental facilities at ELBE is given in Ref. [27].

While in early measurements with timing RPCs at ELBE a scattering setup was used [36], recently, a single-electron mode has been developed by attenuating the beam current down to attoamperes, thus allowing detector testing directly in-beam. This mode has been used to demonstrate the rate capability of ceramic-based MRPCs [37]. The measurements presented in this paper were obtained with an electron beam with a micro-pulse repetition rate of 6.5 MHz and a kinetic energy of 30 MeV. At these energies, electrons have an energy loss similar to that of minimum ionizing particles [38]. A very short bunch duration makes it possible to use the radio frequency (RF) signal of ELBE as the time reference for TOF measurements, thus no start counter is required.

4.2. Experimental setup

The experimental setup was already used in previous studies [22,37] and a simplified scheme is shown in Fig. 5. All detectors were aligned with the help of a stationary laser system. The MRPC was embedded in a scintillator chain aimed at selecting straight electron tracks. The MRPC and scintillator S_5 were both placed on a moving platform, which allows 50 cm movement both in the vertical and horizontal directions via remote control. Thus, a two-dimensional position scan was feasible during irradiation. A trigger condition was required in the form of $S_1\hat{}S_2\hat{}S_3\hat{}S_4\hat{}$RF (3 of the used scintillators have a double-end readout denoted by even and odd numbers, correspondingly, see Fig. 5).

The time-of-flight is defined through the text as the time difference between the MRPC and RF signals. The RF and RPC discriminated signals are fed into a time-to-digital converter (TDC, V1290N) with a least-significant bit (LSB) of 24.5 ps, which yielded an overall resolution of 35 ps/channel (measured from the time difference between a signal split into two different channels). Due to the short 5 ps-bunch we assume hereafter that the resolution of the reference time is dominated by the TDC resolution alone, that will be subtracted in quadrature; thus, strictly speaking, the RPC time resolutions given in this work represent upper bounds provided we have no direct handle on the intrinsic RF signal jitter. Since opto-couplers were used to transmit the signal from the RF cavities up to a transducer that was placed at nearly 2 m distance from the TDC, we do not expect sizeable effects that might arise from loss of signal quality of the (reference) RF signal during transmission.

Following calibration in conditions of δ-impulse excitation, it was estimated that the signal charge was pre-amplified by a factor of 80 in the front-end electronics and by a further factor of 10 in an auxiliary amplifier module. The amplified charge signal was then fed into a 25 fC/channel charge-to-digital converter (QDC, CAEN V965) and integrated over a 50 ns gate. The data acquisition was operated on a GSI multi-branch system (MBS) [39].

4.3. Determination of the particle flux and beam profile

The beam-profile was determined during the experiment by replacing the MRPC under study by a 5 mm-diameter finger-scintillator S_5 that scanned the electron beam vertically and horizontally in self-trigger mode. A high Gaussian beam of width $\sigma_{scint}=1.1$ cm (hor) $\times$ 1.5 cm (vert) was found under these conditions (shown as a continuous line in Fig. 6(a) and (b)) and the single-electron peak could be clearly seen on the scintillator charge distributions. This implies that the experimental situation corresponds to a single-electron per bunch operating mode, as desired.

In view of the narrow beam and the expected large multiple scattering of low-energy electrons, we performed an independent determination of the beam-profile by using the RPC time-difference from the two ends of the strip counter. For that, the signal propagation velocity was previously obtained by fitting the centroid distribution at different RPC positions, yielding a signal propagation velocity of $v=185$ μm/ps. The results are shown in Fig. 6(a), showing a broader distribution with $\sigma_{x,RPC}=1.8$ cm (hor) under RPC self-triggered conditions, while a narrower width of 1.4 cm (hor) was determined under standard trigger conditions $S_1\hat{}S_2\hat{}S_3\hat{}S_4\hat{}$RF, possibly due to the confining effect of the scintillator chain. These two observations give support to the fact that the observed $\sigma_{x,RPC}=1.8$ cm width has little contribution coming from the RPC time resolution (that was previously measured for similar counters + FEE to be less than $\sigma_{x,RPC}=0.8$ cm). By assuming that the broader distribution observed over the RPC comes from multiple scattering, and that the broadening effect is common to the vertical and horizontal directions, a rough estimate of the beam-width at

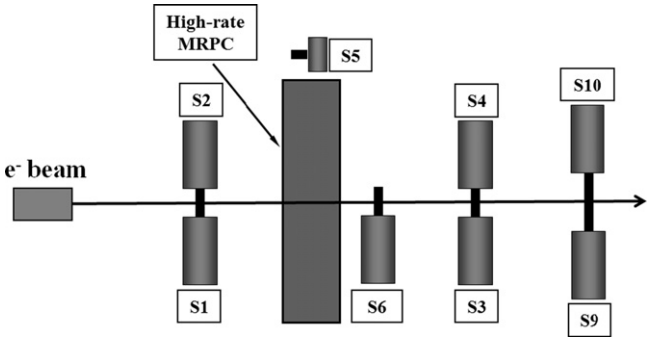

Fig. 5. Schematic view of the RPC test setup. The beam trigger was defined by the coincidence $S_1\hat{}S_2\hat{}S_3\hat{}S_4\hat{}$RF. Together with the MRPC, a small scintillation counter S_5 (finger) was mounted at a step-motor driver to measure the beam size. Counter S_9/S_{10} is a 4 cm-thick scintillator used for monitoring the single-electron distribution of the bunches.

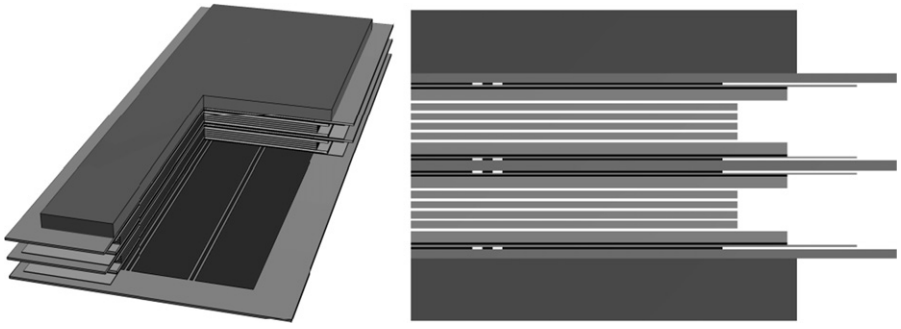

Fig. 4. Strip-readout MRPC, featuring a 10-gap 3-strip structure.

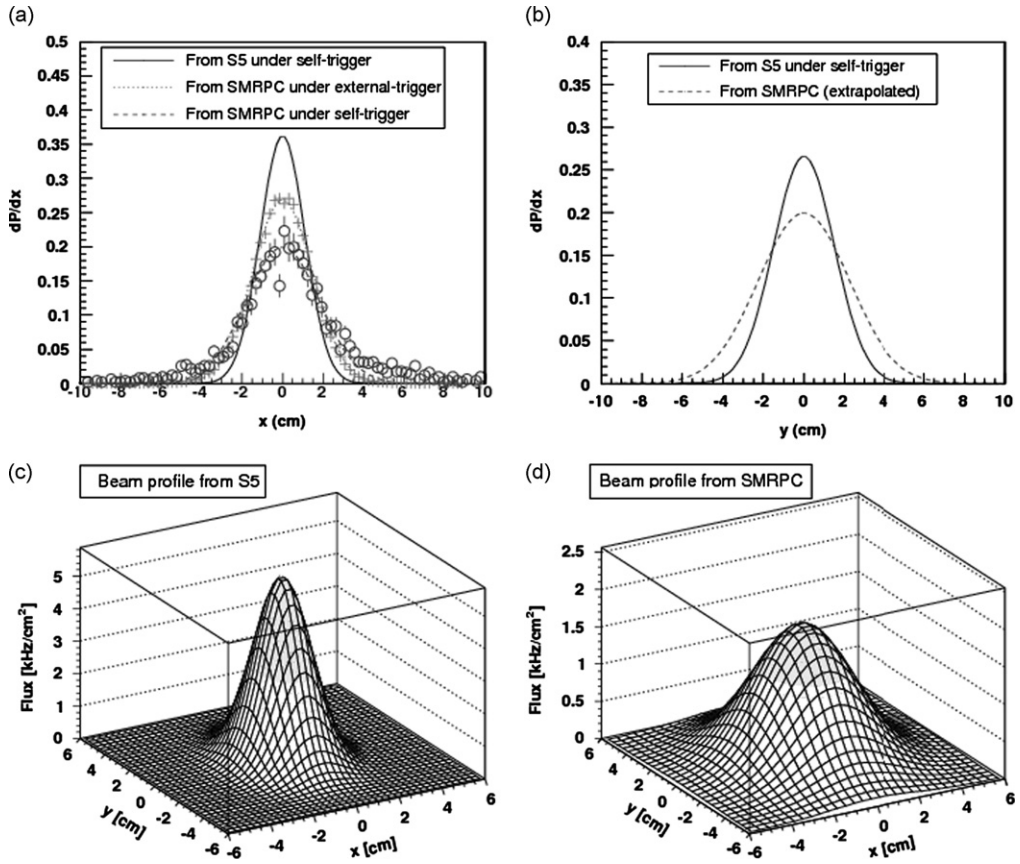

Fig. 6. Beam profiles obtained with the finger scintillator S_5 and with the strip MRPC. (a) Along the strip direction (x), that is parallel to the floor: determined by S_5 (continuous line), by the MRPC under the external scintillator trigger (dotted/crosses) and by the MRPC itself in self-trigger (dashed/circles). (b) S_5 profile perpendicular (y) to the floor (continuous) and extrapolated profile at the RPC (dashed), by assuming multiple scattering. (c) 2-D beam profile determined by S_5 under an electron rate of 5.4 kHz. (d) 2-D beam profile determined by the MRPC at the same counting rate and location.

the RPC position can be made as σ_{RPC}=1.8 cm (hor) × 2.0 cm (vert) (over-estimated by less than 10% in each dimension if the finite RPC resolution is taken into consideration). The implications of the different beam sizes characterized through σ_{scint} and σ_{RPC} are subject of scrutiny in Section 6.

As shown, the beam-profile utilized in this experiment is fairly narrow, and there is indeed some historic controversy on whether the results obtained under this non-uniform situation can be safely extrapolated to the uniform situation [40,41], that is usually of higher practical interest. A natural interpretation for this discrepancy is based on charge diffusion over the resistive plates, but it is not evident that it can have an impact at the cm-scale [19,21,42], that is of interest here. In the following we will assume that charge diffusion is not relevant in the present situation and will follow the analysis procedure sketched in Ref. [33]. Hence, in order to deal with the non-uniformity of the beam, we resort to the average flux $\overline{\phi}$, defined as the expectation value of the local flux $\phi(x,y)$ weighted with its corresponding probability distribution function, $p(x,y)\propto\phi(x,y)$:

$$\overline{\phi} = \iint_{AOI} \phi(x,y)p(x,y)\,dx\,dy = \int_{x_2}^{x_2}\int_{y_1}^{y_2} \frac{r}{2\pi\sigma_x\sigma_y} e^{-((x^2/2\sigma_x^2)+(y^2/2\sigma_y^2))} \frac{\alpha}{2\pi\sigma_x\sigma_y} e^{-((x^2/2\sigma_x^2)+(y^2/2\sigma_y^2))}\,dx\,dy \quad (1)$$

where

$$AOI: \begin{cases} x_1 < x < x_2 \\ y_1 < y < y_2 \end{cases}$$

The normalization factor α is of the order of 1 for the typical integration bounds considered here, to which we refer hereafter as the 'area of interest (AOI)'. The AOI is chosen depending on the region considered for obtaining a certain observable (efficiency, resolution, etc). For the efficiency estimate, the AOI is chosen as the whole effective area of the counter; while for the resolution estimate, the AOI is chosen as the area of one readout cell. The beam rate r is obtained from the first scintillator upstream S_1/S_2 that is known to be large enough to practically contain the entire beam spot at its location.[2] Within the range that is of interest in this work, the S_1/S_2 rates showed a linear response with the luminosity, better than 10%.

Importantly, as demonstrated in Ref. [33], if the charge diffusion over the electrodes can be neglected, the average flux defined through Eq. (1) represents a most convenient choice: namely, it allows to directly relate the detector performance under non-uniform irradiation (subscript n–u) to the one foreseeable in a situation where the flux (ϕ) would be uniform (subscript u) over the entire counter, through the equivalence

$$\varepsilon_{(n-u)}(\overline{\phi}) \equiv \varepsilon_{(u)}(\overline{\phi}) \equiv \varepsilon_{(u)}(\phi);\quad \sigma_{t(n-u)}(\overline{\phi}) \equiv \sigma_{t(u)}(\overline{\phi}) \equiv \sigma_{t(u)}(\phi)$$

This fact makes the interpretation of the present results straightforward and independent from the actual beam shape. A short compilation of these results can be found in (Appendix A).

[2] Exposure of films is periodically done S_1/S_2 upstream for experiments at ELBE. The fact that the beam 'fits' inside S_1/S_2 was checked in present measurements by comparing the self-trigger rates determined from the strip RPC and S_1/S_2, showing an agreement better than 10% at low rates.

At this point, the beam profile used for the analysis is the one determined with the finger scintillator S_5, following the choice made in previous studies with ceramic-based RPCs [37], and allowing for easier cross-comparisons. It has to be noted that for infinite integration bounds (large AOI) and perfectly Gaussian profiles, Eq. (1) yields

$$\overline{\phi} = \frac{r}{4\pi\sigma_x\sigma_y}. \quad (2)$$

In practical terms, the choice of an 'effectively irradiated area' $A^*=4\pi\sigma_x\sigma_y$ allows relating the particle rate with the average flux, under Eqs. (1) and (2). Different choices of the effective area naturally translate into different estimates of the flux. Thus, in the present experimental situation a systematic uncertainty exists, of the order of

$$\frac{\overline{\phi}_{scint}}{\overline{\phi}_{RPC}} = \frac{A^*_{RPC}}{A^*_{scint}} \cong \frac{\sigma_{x,RPC}\times\sigma_{y,RPC}}{\sigma_{x,scint}\times\sigma_{y,scint}} = 2.3$$

($\sim$1.9 if accounting for the finite RPC resolution), slightly dependent on the chosen AOI. We will come back to this relevant issue in Section 6.

4.4. Data analysis

The data analysis has been performed following the algorithms in Ref. [24]. The efficiency is defined as the number of RPC events with valid time signal in at least one cell (either strip or pad) and both its two readout ends (in the strip-readout case) divided by the number of triggered events. In the particular case of the pad counter, since its area does not fully contain the beam in the vertical direction, an auxiliary thin scintillator (S_6) was used to reduce the trigger area in order to obtain the scaling factor for the efficiency ($\times 1/0.85$). Regarding the time resolution, due to the multi-cell environment, there are several ways of obtaining the time resolution by differently weighting the time registered by all fired cells (average, weighted average, fastest, to mention some). We chose here a direct method based on taking the time from the cell with the highest charge (or the two-end average time in the case of the strip counter). In this way we avoid any differential analysis as a function of strip-multiplicity, which would require otherwise a separate communication. We select the cell best centered with respect to the beam-profile and define the AOI at its bounds. So, a 'cell resolution' is given. Obtaining the time resolution over the whole counter by applying this procedure to each cell is a tedious, albeit straightforward, technical matter, that is of relevance in the final system, but that we have not included in this analysis, for simplicity.

Finally, very soft cuts were performed on the scintillator charges, in order to select electrons with similar energy deposits. This has little or no effect on the RPC performance. Fig. 7 shows the typical time-charge slewing correction and the time distribution of the pad MRPC. The average particle flux is 28(17) kHz/cm^2 as obtained from the S_5 scintillator (RPC).

5. Experimental results

5.1. HV scan

MRPCs were conditioned under high voltage for a few hours in order to reach a stable, low dark-rate working regime. The

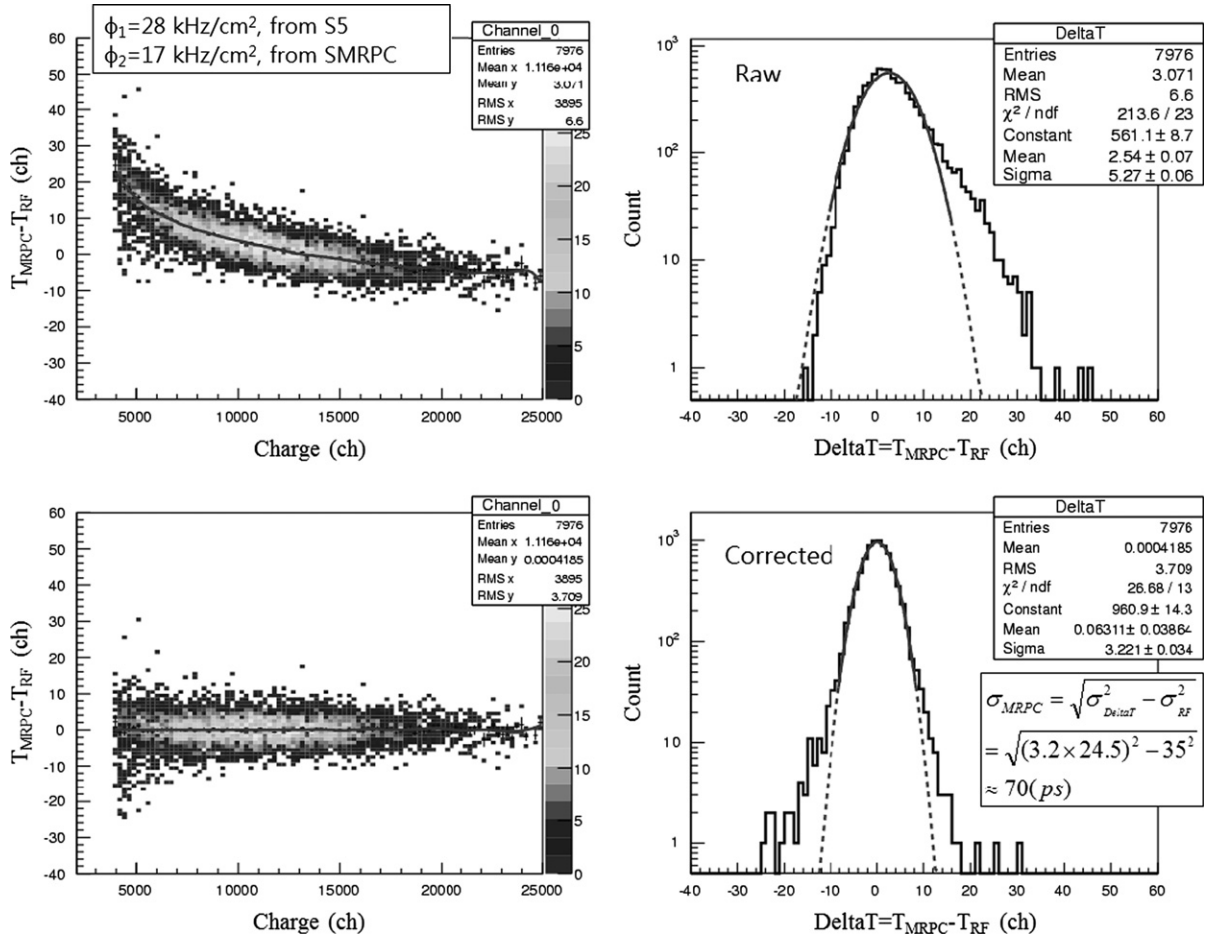

Fig. 7. Typical T–Q correction and time distribution of the pad-readout counter (PMRPC). Up: raw T–Q correlation and time distribution. Bottom: T–Q correlation and time distribution after slewing correction.

electronics threshold was set at 30 mV (for δ-impulse excitation it translates to $q_{th}=30$ fC). The dark rate of the strip module (SMRPC) was about 3.5 Hz/cm^2 at 109 kV/cm, while that of the pad module (PMRPC) was around 10 Hz/cm^2 at 110 kV/cm. Both counters showed dark currents below 0.13 nA/cm^2. It has to be noted that, despite the approximate 10-fold increase of the dark rate as compared to that of float glass ($\sim$1 Hz/cm^2) it remains a factor $\times$1000 below the typical working flux of future high-rate applications. For this glass, as for float glass, the origin of the dark rate (in marked excess with respect to that expected from natural background radiation) is poorly understood at the moment.

In order to find the optimum working voltage of the counters, the efficiency and time resolution were scanned as a function of the applied voltage for a 'low' flux of $\overline{\phi} \sim 2-5$ kHz/cm^2. The results are summarized in Fig. 8. The counters exhibit a comfortable operating 'plateau', simultaneously providing efficiency above 95% and time resolution below 65 ps over as much as 600 V variation in HV. Such a plateau allows for a convenient (and sufficient, for the intended application) 10% tolerance against gas density fluctuations due to uncontrolled environmental conditions (arising mainly through pressure variations that modify the reduced field *E/P*). The intrinsic RPC resolution can be obtained after subtracting the contributions of the FEE and TDC as obtained from pulser measurements. A crude estimate of the resolution down to $\sigma_{RPC}\sim$50 ps is obtained from this approximate procedure.

Although a precise position scan is hardly accessible to a low-energy electron beam, we performed a generic study of the dependence of the RPC performance with position within our (limited) trigger conditions, obtaining a statistical spread of 71.5 ± 3.5 ps at 25 kHz/cm^2 when combining the performance of all 12 pads as measured in separate runs (Fig. 9). Pad-efficiency is more sensitive to beam-detector misalignment and geometrical inefficiency, however the counter efficiency was observed to be well within a 2% variation when the trigger was centered with respect to any of the four central pads. We note that the effective area A^* over which the rate is spread (Eq. (2)), extends well beyond the pad boundaries (pad area$=$ 2.2 cm $\times$ 2.2 cm$=$4.84 cm^2, $A^*=4\pi(1.1\text{ cm}\times 1.5\text{ cm})=20$ cm^2) and therefore the present conditions represent, for low rates, a reasonable first-order approximation to the counter performance under the final uniform use-case, as far as the effect of signal loss arising at the cell boundaries is concerned. Counter non-uniformities, beyond this intrinsic limitation of multi-cell readouts that stems from the shape of the induction profile, can be shown to be small through the aforementioned pad scan and results admit a direct extrapolation to the strip counter, due to the similar architecture.

Last, the pad counter showed an anomalously high cluster size (average number of cells fired per primary electron) of 1.4 at typical working fields (for a relative position beam-chamber as shown in Fig. 9). This was traced (through a dedicated oscillogram study) to 5 ns-period oscillations in the signal base-line, therefore having in all likelihood an electronic origin (signal transit time in the pad is around 100 ps). Despite the cluster size resulting from this oscillating cross-talk is still inferior or comparable to other proposals for the CBM experiment, we intend to minimize it by improving the quality of the connection from the counter to the electronics in near future. Electronics (ASIC-based) and connections will be different in the final system (see Ref. [17] and references therein).

5.2. Rate scan

In order to study the rate capability of the MRPC modules, the counters were tested as a function of the electron flux. The average flux is defined by Eq. (1), with the beam profile estimated from the finger scintillator S_5. For efficiency estimates we take as the AOI the whole active region of the counters, while for the time and charge distributions we restrict the AOI to the cell best centered with respect to the beam profile.

The evolution of the prompt charge distribution for the most central cells can be seen in Fig. 10 for both MRPCs. The pad and

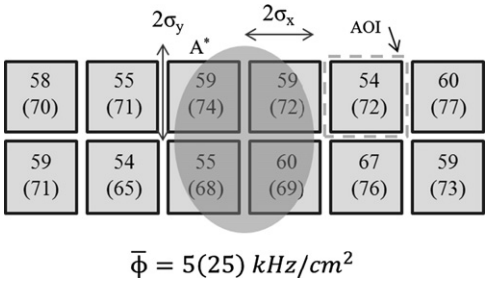

Fig. 9. Time resolution for each pad at 2 typical particle fluxes (5, 25 kHz/cm^2). The beam profile (represented by a shadowed oval) has been chosen for all these measurements to be centered with respect to the pad under study (by remotely moving the platform on which the RPC was sitting). The AOI used to estimate the quoted average flux, $\overline{\phi}$, is illustrated with dashed lines. Except for the pad scan (whose numerical results are shown in figure), the actual relative alignment beam-chamber for all measurements of the pad response presented in this work is the one sketched in the figure (and similarly for the strip counter). The AOI for the flux determination in the efficiency study is taken to be the full active size of the detector itself.

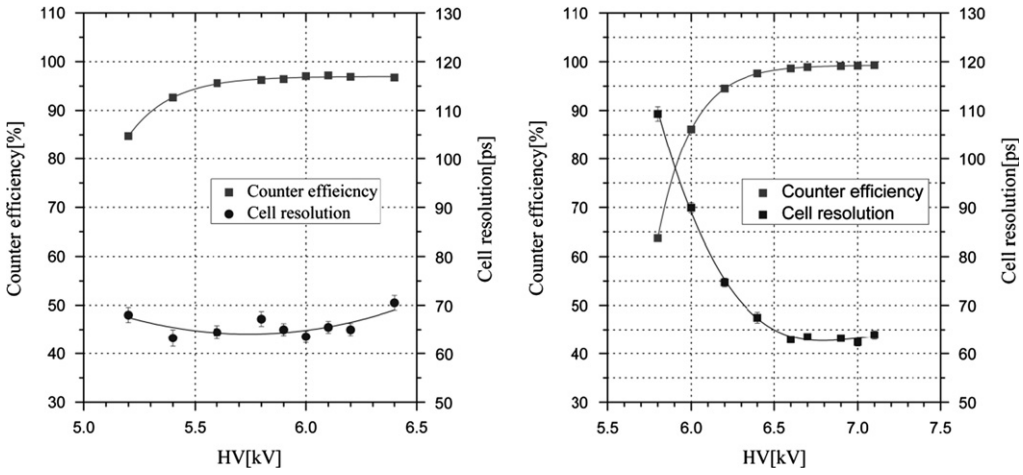

Fig. 8. Efficiency and time resolution as a function of high voltage (HV). Left: HV scan for the pad-readout module (PMRPC) at an average electron flux of 1.9 kHz/cm^2. Right: HV scan for the strip-readout module (SMRPC) at an average electron flux of 5.4 kHz/cm^2.

strip MRPCs were operating under electrical fields of 109 kV/cm and 103 kV/cm (6.0 kV and 6.45 kV in Fig. 8), respectively. For the strip MRPC, the charge is obtained from the sum of its two ends. It can be seen that, with the increase of the electron flux, the average charge for both counters decreases and the spectrum shifts down to low charges as expected. Limited by the beam time schedule, we could not take data files at high particle flux for the strip counter operated at an optimal field of 108 kV/cm (6.75 kV in Fig. 8-right) and performed the study at just 6.45 kV. This departure from the center of the efficiency plateau toward its left end (sitting at 6.2 kV for a 5% efficiency drop; Fig. 8-right) made the strip counter in this work unrealistically sensitive to the dynamic voltage drop arising at high flux (that shows an approximate linear behavior with φ: see for instance Eq. (4) or Ref. [17] for a detailed account).

The high-flux behavior of the efficiency and time resolution for the two modules are shown in Figs. 11 and 12. As said, due to the limited beam time, not all combinations in parameter space could be investigated and the data files for the open symbols in Fig. 11 (at increased field) were absent. Accordingly, it is impossible to obtain the time resolution or efficiency for these runs. Nevertheless, the detector current and rates were recorded so we can provide an estimate of the efficiency through it, based on a simple DC model. A natural consequence of this physical image is that both the efficiency and charge distributions depend on the effective field in the gap after correcting for the dynamic DC voltage drop at the resistive plates. Hence, the efficiency depends strongly on the average charge (i.e., the gain), and the latter can be estimated from the current. Taking the data during the HV scans as a reference, we extrapolate the efficiency for the given total charge in a crude way. Although this procedure cannot replace a direct measurement, it is good enough to obtain a reasonable expectation. The DC model and the definition of the total charge will be described in the following section. It can be seen in Figs. 11 and 12 that the maximum tolerable particle flux approaches the 100 kHz/cm^2 land-mark for these counters based on low-resistive glass, reminiscent of the behavior observed for ceramic counters under similar conditions [37].

From the indirect analysis (open symbols), it can be seen that the strip counter under an electric field around 108 kV/cm (circles) is expected to show a higher efficiency at high particle flux, which suggests that the counter performances could still be improved by optimizing the working voltage.

6. Discussion

As described in Section 4.3, the beam-profile was determined independently through a finger-scintillator (S_5) and the MRPC itself. An obvious discrepancy between the two estimates can be observed (Fig. 6). By using the simple multiple scattering formula from Ref. [43], we obtain a width of $\sigma_x=\sigma_y=1$ cm, for a point-like 30 MeV electron beam at S_1/S_2, considering its thickness (0.5 cm, PVT) and lever arm (23 cm distance between S_1/S_2 and the RPC). This is fairly consistent with the values measured by the finger sicintillator S_5 placed at the RPC position ($\sigma_x=1.1$ cm, $\sigma_y=1.5$ cm). To interpret the influence of RPC ($\sigma_x=1.8$ cm, $\sigma_y=2.0$ cm) with simple formulas is more difficult, since the RPC itself is active. Taking the formulas at face value, the observed spread would require having an additional 1.5 cm Al-equivalent material budget with an increased lever arm by around 6 cm. These numbers exceed by some 50% a naive expectation from the known materials and dimensions of the chamber but can be considered reasonable,

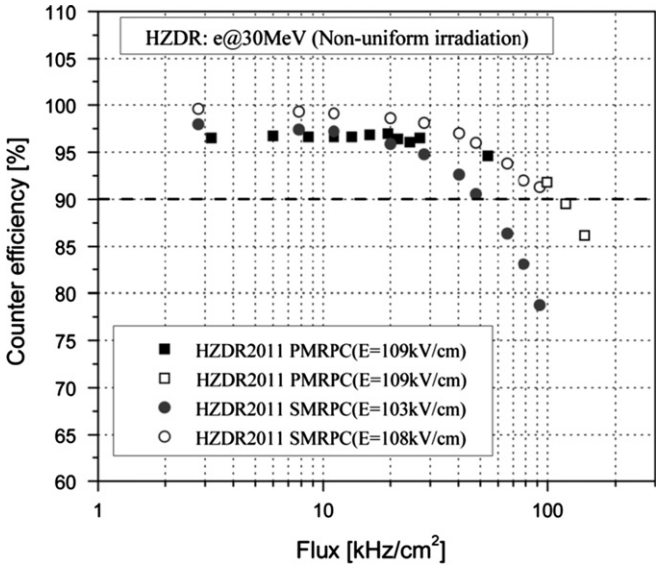

Fig. 11. Measured efficiencies for different runs as a function of the average particle flux determined with reference scintillators. Open symbols are obtained through an indirect analysis that is described in the text.

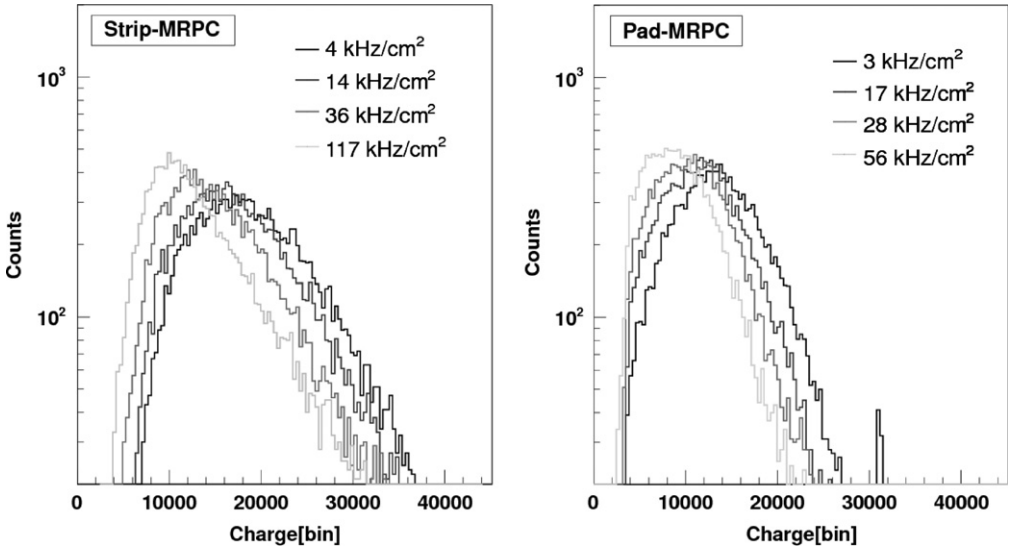

Fig. 10. Charge distribution at different flux over one readout cell. The field is 103 kV/cm for the strip counter and 109 kV/cm for the pad counter.

in view of the limited scope of the analytical formulas. Since the position resolution from the RPC alone is at 0.8 cm level, it is plausible that this additional spread is mainly caused by multiple scattering in the RPC.

As previously noted, there is indeed some controversy on whether the results obtained under non-uniform conditions can be extrapolated to an uniform situation, a natural interpretation for this discrepancy being the diffusion of the avalanche charge over the resistive plates. The phenomenon is expected to occur, although at a scale significantly smaller than the cm-scale that is of interest here. However, even if charge diffusion could be neglected, there is still some degree of sophistication needed in order to properly interpret the results in light of the uniform situation, and an operative approach to the problem has been recently described in [33]. In order to properly address the case we split the discussion in two parts.

6.1. Rate capability and locality

If charge diffusion is of importance, it can be expected that the local detector behavior will be little dependent on the local value of the particle flux. As an example, if it is (unrealistically) assumed that charge diffusion over the surface of the resistive plate is an instantaneous process, the total charge released would uniformly distribute over the complete detector, of area A. The effective particle flux would be $\phi = r/A$, usually much smaller than the plausible estimate $\phi = r/A^*$ (from Eq. (2)) for any practical non-uniform situation. As a result, the observable response of the counter (efficiency, time resolution) would be uniform everywhere, and would correspond to the response to a particle flux artificially reduced by A^*/A; rate capability would be over-estimated precisely by this factor. Conversely, if the RPC response would show a strong local behavior, charge diffusion might be excluded, at least qualitatively.

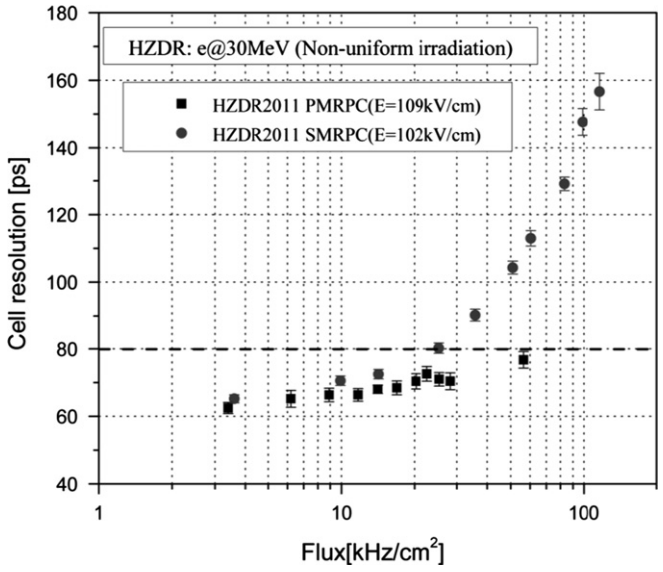

Fig. 12. Measured time resolutions for the cell with highest statistics (centered with respect to the beam) as a function of the average particle flux determined with reference scintillators.

In order to study the locality of the RPC response it is most convenient to study the detector gain as a function of its position, and to see whether it is related to the value of the incoming local flux or not. This is strictly not possible for an RPC in the present situation because: (i) RPC electronics usually senses the fast/prompt charge, not the gain and (ii) there is no external position-sensitive detector in the present setup. An alternative approach is sketched as follows.

First, the avalanche fast charge, q_{fast}, is obtained from the QDC (after calibration) as a function of the position along the RPC strip counter, determined with the RPC itself, at a reference electrical field of 103 kV/cm (Fig. 13-left). It is indeed possible to approximately translate the fast charge to total charge by assuming that they are functionally related in a way that is independent from the particular voltage and particle flux. So a calibration curve q_{fast}–q_{tot} can be obtained from the low-flux HV-scans of Fig. 8, for which the current was monitored, by using

$$q_{tot} = \frac{1}{2}\frac{I}{r} \tag{3}$$

This relation holds for mirrored RPCs (with up–down symmetry, like the ones studied here) with r being the particle rate. Fig. 13-right shows the total charge (q_{tot}) of the counter, in response to an electron that hits the RPC in a certain position, obtained by this procedure. In this step (q_{fast}–q_{tot} calibration) we are arguing along the lines of the DC model, but this assumption is not instrumental for the evaluation of the locality of the RPC response that follows. The reason for the choice of q_{tot} is that, being related to the gas gain through the average number of primary electrons released per gap $m = q_{tot}/n_0 \sim 5 \times 10^6$ it readily allows for interpretation of the final result based on the conventional DC model, as will be shown.

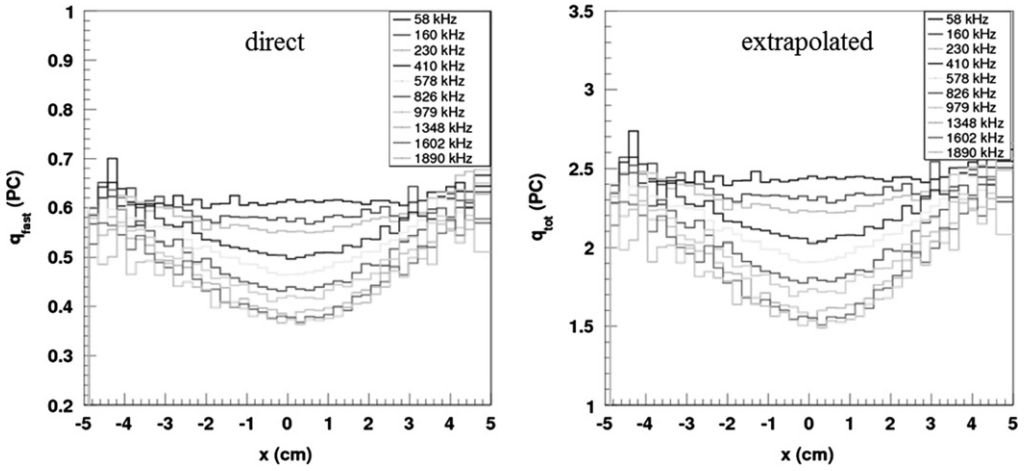

Fig. 13. Left: fast charge as a function of the RPC position for different rates. Right: same figure, for the total charge after applying the extrapolation procedure described in text. (We have re-studied our earlier data and confirmed that a number of errors resulted in a previous under-estimation of the average charge down to 1 pC for typical working conditions, as given in [24]. A figure $q_{tot} \sim 2$–2.5 pC at the typical operating point is more adequate for our architectures.)

We have two independent estimates of the profile of the impinging beam (from RPC and S_5), that scale roughly proportionally with the beam luminosity at every position as shown in Fig. 14-up. A third case, the profile obtained under trigger conditions, is also shown for illustration. The total charge as a function of the local value of the flux for each of the three different ansatz is shown in Fig. 14-down. In the case of the RPC-profile ansatz, an universal behavior is observed (Fig. 14b(1)), while the scintillator-profile (Fig. 14b(3)) clearly shows strong deviations. Under trigger conditions (Fig. 14b(2)), for which the charge has indeed been obtained, the agreement is not good. Moreover, the best agreement in Fig.14b(1) requires taking into consideration small instabilities of the beam that affect its width at the 10% scale, differing from run to run.

A last hint of the correctness of the scaling observed in Fig. 14b(1) might be obtained by resorting to the DC model under the lineal q_{tot} vs. E approximation (Ref. [19], for instance). For the case of multi-gap, the average field in the gap can be then expressed as

$$\overline{E}_{gap} = E_{th} + \frac{(E-E_{th})}{(1+a\phi\rho d^*/g)} \tag{4}$$

with

$$d^* = d(N+1)/N \tag{5}$$

being $\overline{E}_{gap}$ the average field in the gap, ϕ the particle flux, ρ the bulk resistivity of the glass plate, g the thickness of the gap and N the number of the glass plates between positive and negative HV electrodes. $\overline{E}_{th}$ and a are the parameters characterizing the $q_{tot}(E)$ relation at zero flux as $q_{tot,0} = a(E-\overline{E}_{th})$. d^* is defined as the average glass thickness per gap in the case of a multi-gap structure. The total charge at finite flux can be obtained as

$$q_{tot} = \frac{a(E-E_{th})}{1+a\phi\rho d^*/g} \tag{6}$$

In Eq. (6), the only free parameter is the bulk resistivity ρ and all the others can be obtained from the experimental data. So it is possible to apply the DC model to the data points in Fig. 14b(1) in order to extract a value for the resistivity. The model is shown as the continuous line, with a best fit value of $\rho = 2.6 \times 10^{10}\ \Omega\ cm$, compatible with the value directly measured in Fig. 1 when extrapolated to 19 °C.

The above observations leave little room for charge diffusion or other non-local effect to be important at the cm-scale for the type of glass used in these counters. We have to admit, however, that there is a limitation insofar as we do not have a good independent estimate of the beam shape, other than that by the RPC itself. It seems to us that the most plausible interpretation of the present situation is that there is indeed multiple-scattering in the RPC, and that, once taking into account the additional broadening, the counter properties depend merely on the local situation.

6.2. Comparison with earlier results for the case of uniform irradiation

It has been shown in Ref. [33] that, under the assumption of locality, a direct extrapolation to the rate capability expected in the uniform case can be performed by simply resorting for

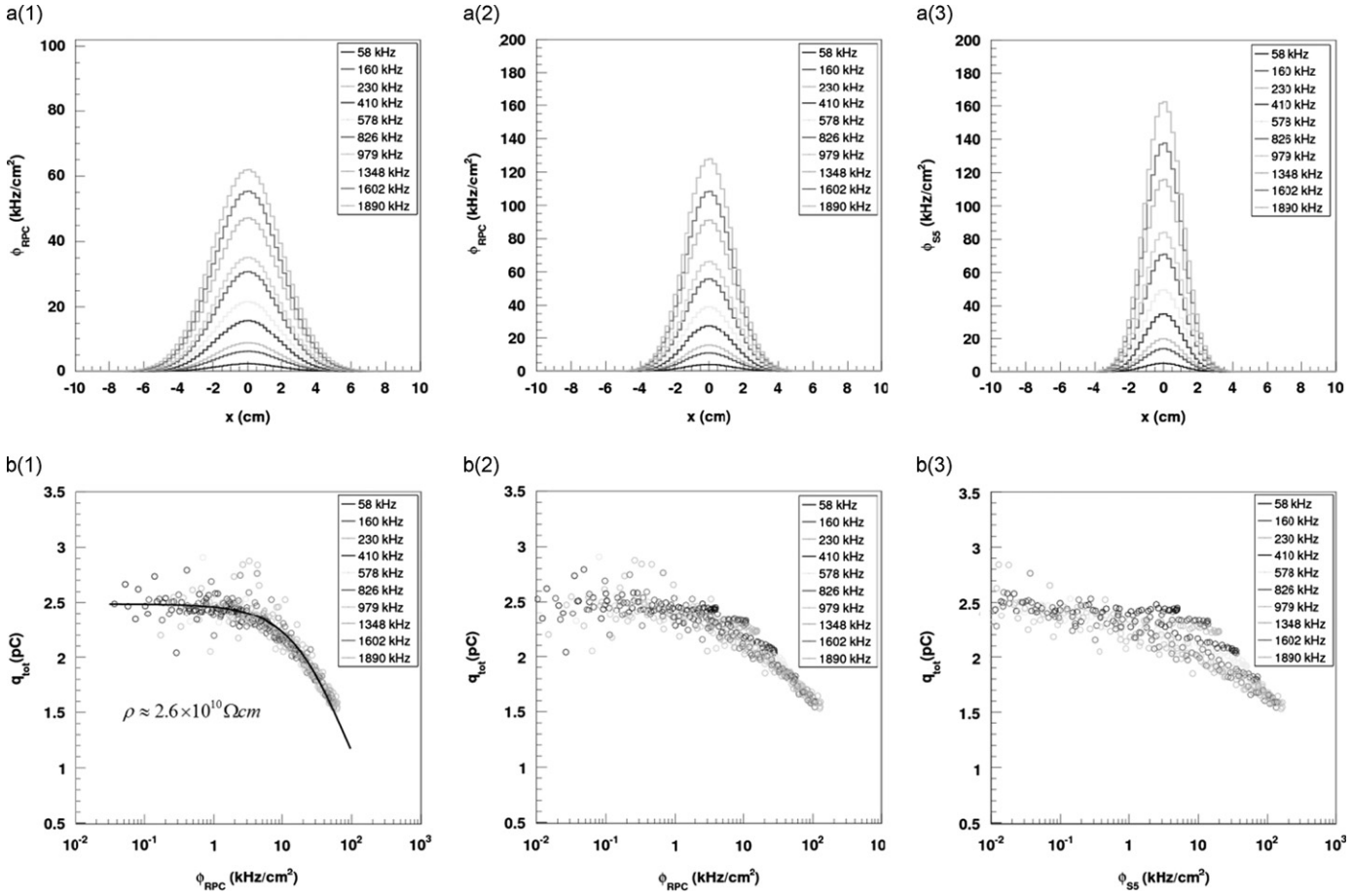

Fig. 14. Compilation of the counter behavior for the strip MRPC, under different assumptions on the beam profile. Up: local flux as a function of position determined from (a1) the RPC itself. (a2) the RPC under an external scintillator trigger given by S_1^S_2^S_3^S_4^RF, (a3) a finger scintillator S_5 at the RPC position (RPC removed). Down: correspondingly, total charge as a function of the local flux as obtained by resorting to the profiles obtained in (a1), (a2) and (a3). A fit to the DC model leaving the glass resistivity as the only free parameter is overlaid in (b1).

representation to the average flux, $\overline{\phi}$, defined over the same AOI over which the observation is studied. Therefore, if the above interpretation based on the additional broadening due to multiple-scattering of the impinging electrons on the RPC structure is correct, the rate capability reported in Section 4.3 is overestimated by a factor around $\overline{\phi}_{scint}/\overline{\phi}_{RPC} \cong 1.9$.[3]

In Fig. 15 we compare the counter performance as a function of the particle flux (down-scaled by using the beam profile estimated with the RPC itself, circles in Fig. 6(a)) with our earlier results obtained under a uniform beam [24]. Efficiency from that work has been renormalized to 100% (less than 5% correction) in order to allow for easier comparison.

In all, the present rate capability for the pad counter is higher by a factor $\times 2$ than the one obtained in Ref. [24] for a uniform beam, extending up to 35 kHz/cm^2 (defined as the particle flux for which an efficiency of 90% and a time resolution below 80 ps can be simultaneously achieved). This result can be considered to be in a good agreement, in view of the intrinsic systematic bias of this type of measurement (due to the absence of temperature control, different working HV and gas mixture). We suspect indeed that the better performance can be partly attributed to a better selection of glass, but we have no direct evidence whatsoever. The quality assurance procedure was much softer 2 years ago than it is at the moment.

Results for a different architecture based on this type of glass, also obtained with pencil beams, indicate that good working conditions up to 100 kHz/cm^2 might be indeed achievable [44]. However, since no account is given in that work on the flux determination, we suggest however to take those results with caution.

7. Conclusion

The requirements of the inner-most region of the CBM–TOF wall, namely, 80 ps time of flight resolution at 90% efficiency for a particle flux as high as 20 kHz/cm^2, have been fulfilled by resorting to real-size pad MRPC modules based on the newly developed Chinese doped glass. Moreover, the pad counter prototype can run with a tolerable performance degradation up to 35–60 kHz/cm^2. A low-granularity 3-strip RPC shows a rate capability up to 15–25 kHz/cm^2, sufficient for the coverage of the region for which it has been envisaged. The uncertainty in the quoted flux-ranges is related to the uncertainty in the beam profile due to the observed additional broadening of the electron beam because of multiple scattering in the RPC itself.

As a summary, the developed real-size prototypes (with pad and strip readout) are able to operate within the technical specifications of future time of flight wall of the Compressed Baryonic Matter experiment at FAIR, for a flux at least twice as high as the one expected in the most extreme physical scenario. A reasonable safety margin for operation is thus provided. At the moment we are working on scaling the strip module to a larger size, which should largely simplify the coverage of the final system. An optimization of its working voltage will be pursued, that we expect will allow for a yet improved behavior as a function of the particle flux. Results will be published elsewhere.

[3] In detail, this is true for infinite AOI, that fits well to the efficiency determination. For the time resolution the AOI is restricted to a cell and the correction is slightly smaller by some 10%, differing between the pad and strip counter.

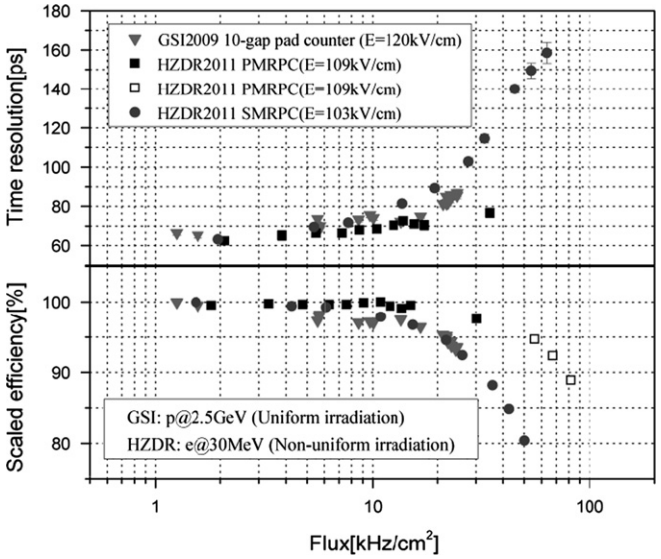

Fig. 15. Compilation of the main results in this work after normalization to 100% efficiency (less than 5% correction). The down triangles show the GSI-SIS data (uniform beam) while the remaining data sets are extracted from the present analysis.

Acknowledgments

We thank the crew of the ELBE linac for providing excellent beam conditions and warm support during the experiment and to D. Yakorev for helpful discussions. We are grateful to the members of the CBM Collaboration for fruitful discussions and their valuable remarks. This work is supported by the National Natural Science Foundation of China under Grant nos. 11020101059, 10775082, 111050110573 and 10979030. It is also supported by the Tsinghua University Initiative Scientific Research Program. This work is supported by the EU under Grant no. 283286 of HadronPhysics3 and by the German BMBF under Grant no. 06DR9059.

Appendix A. Uniform vs. non-uniform irradiation in a purely local scenario

We compile here without proof the main results derived in Ref. [33] with notation slightly modified in order to make them more comprehensive. It is assumed in the following equation that a given detector property (f) depends on position, characterized by sub-indexes i, j, with the usual definition:

$$f_{ij} \equiv \frac{1}{2}\left[f(x_i-\Delta x/2, y_j-\Delta x/2)+f(x_i+\Delta x/2, y_j+\Delta x/2)\right]$$

A distribution of normalized weights can be introduced, based on the local value of the flux ϕ_{ij} as

$$p_{ij} = \frac{\phi_{ij}\Delta x \Delta y}{r}, \quad \sum_{i,j}^{AOI} p_{ij} = 1$$

where AOI stands for the area of interest (over which a certain detector property is evaluated) and r is the total particle rate. It is shown in Ref. [33] that the efficiency and time response variance over the AOI are well approximated by the following formulas:

$$\varepsilon|_{AOI} = \sum_{i,j}^{AOI} p_{ij}\varepsilon_{ij} = \overline{\varepsilon}|_{AOI}$$

$$var_t|_{AOI} = \frac{\sum_{i,j}^{AOI} p_{ij}\varepsilon_{ij} var_{t,\ ij}}{\sum_{i,j}^{AOI} p_{ij}\varepsilon_{ij}} = \frac{\overline{var_t \times \varepsilon}|_{AOI}}{\overline{\varepsilon}|_{AOI}}$$

The flux averaged over the AOI can be at this point tentatively defined as

$$\overline{\phi}|_{AOI} = \sum_{i,j}^{AOI} p_{ij}\phi_{ij}$$

(its continuous form, given by Eq. (1), has been used through the text). If the assumption is made that a certain detector property is nearly-linearly changing with flux (as regularly observed in practice)

$$\varepsilon_{ij} = \varepsilon_0(1-k_\varepsilon\phi_{ij}) \tag{A.1}$$

Multiplying by weight p_{ij} and summing over the AOI leads to

$$\sum_{i,j}^{AOI} \varepsilon_{ij}p_{ij} = \sum_{i,j}^{AOI} \varepsilon_0(p_{ij}-k_\varepsilon\phi_{ij}p_{ij})$$

and finally to

$$\varepsilon|_{AOI} = \varepsilon_0(1-k_\varepsilon\overline{\phi}|_{AOI}) \tag{A.2}$$

that remarkably retains the functional behavior of Eq. (A.1). Similarly for the detector variance, but with approximate character, it can be obtained

$$var_t|_{AOI} \cong var_{t,\ 0}(1+2k_t\overline{\phi}|_{AOI}) \tag{A.3}$$

$$\sigma_t|_{AOI} \cong \sigma_{t,\ 0}(1+k_t\overline{\phi}|_{AOI}) \tag{A.4}$$

The Taylor expansion of Eq. (A.3) given in Eq. (A.4) is extremely accurate due to the slow character of the square root function: an increase up to 100% with respect to the value $var_{t,0}$ at zero flux in Eq. (A.3) yields less than a 10% error in Eq. (A.4). Actually, despite measured trends may not be perfectly linear functions (A.2)–(A.4), it was shown in Ref. [33] that the following relations represent excellent approximations to the behavior of measured data

$$\varepsilon|_{AOI} \equiv \varepsilon|_{AOI}(\overline{\phi}|_{AOI}) \tag{A.5}$$

$$\sigma_t|_{AOI} \equiv \sigma_t|_{AOI}(\overline{\phi}|_{AOI}) \tag{A.6}$$

that is, the behavior of efficiency and time resolution as a function of the average particle flux is independent from the actual beam shape: therefore, it does not depend on the distribution of weight p_{ij} and in it will be the same for the case of uniform irradiation (where $\overline{\phi}|_{AOI} = \phi_{ij}$ for all i, j) as for any general non-uniform situation. An operational analysis rule can be extracted as follows: *in order to estimate a detector property under non-uniform high irradiation conditions it is convenient to study the detector property as a function of the average flux, both (property and flux) evaluated over the same AOI. Upon application of this rule, the result coincides with the one expected under uniform irradiation, allowing for easier interpretation.* Any AOI can be chosen, although for efficiency estimates it is convenient that it is larger than the trigger region.

References

[1] E. Cerron Zeballos, et al., Nuclear Instruments and Methods A 374 (1996) 132.
[2] P. Fonte, et al., Nuclear Instruments and Methods A 443 (2000) 201.
[3] P. Fonte, et al., Nuclear Instruments and Methods A 449 (2000) 295.
[4] A.V. Akindinov, et al., Nuclear Instruments and Methods A 533 (2004) 93.
[5] D. Hatzifotiadou, Nuclear Instruments and Methods A 502 (2003) 123.
[6] A. Akindinov, et al., Nuclear Instruments and Methods A 533 (2004) 74.
[7] A. Akindinov, et al., Nuclear Instruments and Methods A 602 (2009) 709.
[8] B. Bonner, et al., Nuclear Instruments and Methods A 478 (2002) 176.
[9] B. Bonner, et al., Nuclear Instruments and Methods A 508 (2003) 181.
[10] Yi Wang, et al., Nuclear Instruments and Methods A 613 (2010) 200.
[11] M. Petrovici, et al., Nuclear Instruments and Methods A 487 (2002) 337.
[12] A. Schüttauf, et al., Nuclear Instruments and Methods A 533 (2004) 65.
[13] H. Alvarez Pol, et al., Nuclear Instruments and Methods A 535 (2004) 277.
[14] D. Belver, et al., Nuclear Instruments and Methods A 602 (2009) 687.
[15] S. An, et al., Nuclear Instruments and Methods A 594 (2008) 39.
[16] D. Bartos, et al., IEEE NSS/MIC 2008, Book Series, in: Proceedings of IEEE Nuclear Science Symposium, vol. 1–9, 2008, p. 1933.
[17] I. Deppner, et al., Nuclear Instruments and Methods A 661 (2012) 121.
[18] C. Gustavino, et al., Nuclear Instruments and Methods A 527 (2004) 471.
[19] D. Gonzalez-Diaz, et al., Nuclear Instruments and Methods A 555 (2005) 72.
[20] L. Lopes, et al., Nuclear Physics B—Proceedings Supplements 158 (2006) 66.
[21] D. Gonzalez-Diaz, et al., Nuclear Physics B—Proceedings Supplements 158 (2006) 111.
[22] A. Akindinov, et al., Nuclear Instruments and Methods A 572 (2007) 676.
[23] V. Ammosov, et al., Nuclear Instruments and Methods A 576 (2007) 331.
[24] J. Wang, et al., Nuclear Instruments and Methods A 621 (2010) 151.
[25] L. Naumann, et al., Nuclear Instruments and Methods A 635 (2011) 113.
[26] Yu.N. Pestov, Nuclear Instruments and Methods A 196 (1982) 45.
[27] The radiation source ELBE 〈http://www.fzd.de/pls/rois/Cms?pNid=145&pOid=10242〉.
[28] Diego Gonzalez-Diaz, Huangshan Chen, Yi Wang, Nuclear Instruments and Methods A 648 (2011) 52.
[29] Y. Wang, et al., JINST 7 (2012) P11017.
[30] Tapasi Ghosh, et al., Nuclear Instruments and Methods A 661 (2012) S177.
[31] Changguo Lu, Nuclear Instruments and Methods A 602 (2009) 761.
[32] 〈http://www.misumiusa.com/CategoryImages/Metric_2009_pdf/p2839.pdf〉.
[33] J. Wang, et al., JINST 7 (2012) P10004.
[34] F. Geurts, et al., Nuclear Instruments and Methods A 533 (2004) 60.
[35] W.J. Llope, et al., Nuclear Instruments and Methods A 596 (2008) 430.
[36] R. Kotte, et al., Nuclear Instruments and Methods A 564 (2006) 155.
[37] L. Naumann, et al., Nuclear Instruments and Methods A 628 (2011) 138.
[38] D. Yakorev, et al., Nuclear Instruments and Methods A 654 (2011) 79.
[39] H. Essel, N. Kurz, IEEE Transactions on Nuclear Science NS-47 (2) (2000) 337.
[40] I. Crotty, et al., Nuclear Instruments and Methods A 360 (1995) 512.
[41] C. Bacci, et al., Nuclear Instruments and Methods A 352 (1995) 552.
[42] C. Lippmann, et al., Nuclear Physics B—Proceedings Supplements 158 (2006) 127.
[43] K. Nakamura, et al., (Particle Data Group), Journal of Physics G 37 (2010) 075021.
[44] M. Petrovici, et al., JINST 7 (2012) P11003.